
Carrier Beating Impairment in Weakly Coupled Multicore Fiber-Based IM/DD Systems

JIAJIA ZHAO¹, LIN GAN², LEI SU³, JINSHUAI ZHANG³, HAIRONG HE¹, WANGYANG CAI¹, JIN WANG¹, SONGNIAN FU², and MING TANG²

¹School of Computer and Communication Engineering, Changsha University of Science and Technology, Changsha 410114, China

²Wuhan National Lab for Optoelectronics (WNLO) & National Engineering Laboratory for Next Generation Internet Access System, School of Optical and Electronic Information, Huazhong University of Science and Technology, Wuhan 430074, China

³School of Engineering and Materials Science, Queen Mary University of London, London E1 4NS, United Kingdom

Corresponding author: Lin Gan (e-mail: lingan@hust.edu.cn).

This work was supported in part by the National Key R&D Program of China (2018YFB1801002); National Natural Science Foundation of China (NSFC) (61722108, 61931010); and the International Cooperative Extension Program of Changsha University of Science and Technology, China (Grant No. 2019IC35).

ABSTRACT Weakly coupled multicore fiber (WC-MCF) is promising for use in short-reach fiber telecommunication systems in the near future. Intercore crosstalk (XT) plays an important role in WC-MCF-based short-reach intensity-modulation/direct-detection (IM/DD) systems, because XT can significantly degrade system performance. For the first time, the combined effect of intercore XT and the frequency offset between optical carriers, which is defined as the carrier beating impairment (CBI), is measured and characterized by experiments and numerical simulations. The experimental results show that the CBI causes large fluctuations in the signal-to-noise ratio (SNR) with a normally tolerable XT level. Such SNR fluctuations can additionally reduce the system's XT tolerance (at worst 1-dB SNR degradation) by as much as 20 dB for 4-level pulse amplitude modulation (PAM-4) transmission. The simulation results show that the CBI is mainly affected by the specific properties of the laser source and the modulation depth of the transmitted signals. These results suggest that the XT should be designed to be much smaller for WC-MCF-based short-reach IM/DD systems when there is the CBI.

INDEX TERMS Multicore fiber, intercore crosstalk, optical carrier, telecommunication.

I. INTRODUCTION

Driven by the emerging of 5th-Generation network, cloud services, quantum secured network [1, 2], spatial division multiplexing (SDM) technology has grown rapidly over the past decade, from short-reach to long-haul optical fiber telecommunication systems. Weakly coupled multicore fiber (WC-MCF) based intensity modulation/direct detection (IM/DD) systems are very promising for application in low-cost/high density parallel signal-mode core links, ultra-high-density trunk/outside plane cables [3], and intra- or inter- datacenter interconnects [4, 5]. To reach the maximum system capacity, one method is the inclusion of as many cores as possible in the MCF. However, small core pitch introduces large inter-core crosstalk (XT), which can significantly degrade the signal quality. Therefore, it is meaningful to investigate the XT characteristics in WC-MCF-based short-reach IM/DD systems.

Recently, related works about XT in WC-MCF have been mainly focused on two aspects: (i) establishing the physical model for XT and (ii) discussing the impact of XT on

specific transmission systems. For XT modeling, coupled-mode theory with an equivalent refractive index model can be used for heterogeneous WC-MCF [6] and homogeneous WC-MCF [7]. For the time-dependent characteristics of XT, the XT power fluctuations depend on the signal symbol rate, modulation and walk-off between cores [8]. For the frequency-dependent characteristics of XT, the decorrelation bandwidth of the XT power decreases with transmission distance by a fractional linear function that is dominated by the walk-off between cores [9,10].

An accurate mean XT power estimation method has also been proposed with longitudinal variation of the coupling coefficient with bending and twisting taken into consideration [11]. It is observed that temperature, pseudo

random binary sequence (PRBS) length, modulation format and signal rate impact the intensity and volatility of XT [12].

To investigate the impact of XT on specific transmission systems, many studies have been performed. For coherent optical transmission systems, it has been demonstrated that -40 dB XT only has an average penalty below 0.25 dB for the 24.5 GBaud polarization division multiplexing 64-quadrature amplitude modulation (PDM-64QAM) format over 172.8 km 19-core homogeneous WC-MCF [13]. Furthermore, there exists a universal target for the XT level of MCF of approximately -40 dB/100 km that is valid for metropolitan (~100 km) to trans-pacific (~10,000 km) deployment scenarios [14].

For short-reach IM/DD systems, many types of homogeneous [15-17] or heterogeneous [18] WC-MCF have been optimized with different XT threshold. For different kinds of WC-MCF based systems, the XT threshold has been studied, such as adaptive direction-detection orthogonal frequency-division multiplexing (DD-OFDM) signals [19], the on-off key (OOK) signal [20, 21], the 4-level pulse amplitude modulation (PAM-4) signal [22] and the PAM-8 signal [23]. The combined effect of laser phase noise and intercore XT on IM/DD systems has also been investigated [24, 25]. However, the combined effect of inter-core XT and the frequency offset between optical carriers, which we define as the carrier beating impairment (CBI), has not been fully discussed [26]. The main contribution of this paper is summarized as follows:

- 1) The CBI is theoretically discussed and the clear definition of the CBI is proposed.
- 2) The effect of the CBI on the WC-MCF-based short-reach PAM-4 transmission is experimentally confirmed. The equalization algorithm at the receiver can compensate the CBI in some cases.
- 3) Simulation is carried out to evaluate the long-term performance affected by the time-dependent XT, and the specific properties of the laser source.

The rest of this paper is organized as follows. In Section II, two kinds of transmitter schemes are introduced for the MCF-based IM/DD transmission link. The mathematical analysis of the CBI is also presented. Section III gives the experimental results of the measured CBI for the above two schemes. Section IV verifies a new simulation model for optical lasers with frequency dither. The CBI is also numerically investigated in this section. Section V analyzes the impact of the specific properties of the laser source, the modulation depth of the transmission signals, the walk-off of the WC-MCF on CBI.

II. WC-MCF-BASED SHORT-REACH IM/DD SYSTEMS

A. LASER SHARED SCHEME AND LASER NON-SHARED SCHEME

We introduce two types of transmitter schemes for the WC-MCF-based short reach IM/DD systems, namely, the laser

shared scheme and the laser non-shared scheme. Fig. 1 demonstrates the laser shared scheme, which is also utilized in [27]. All the transmitters (including modulator and electrical driver) use one optical laser as the optical carrier (OC). A 1:N optical power splitter is needed to couple optical power into each transmitter. Then, the signals of all the channels are coupled to a N-core MCF via low-loss fan-in/fan-out devices. At the receiver side, each receiver (Rx) operates independently to recover the transmission signals.

Fig. 2 demonstrates the laser non-shared scheme. For example, dense 2-D six-channel vertical cavity surface-emitting laser arrays (VCSELs) can be used with multimode MCF for data center interconnects [28]. Each transmitter uses an independent laser source as the OC. Due to the fabrication and control error, it is impossible for all the laser sources to work at the same optical frequency. Therefore, there are unavoidable frequency offsets among the OCs.

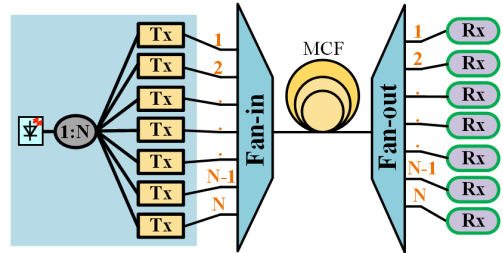


FIGURE 1. The laser shared scheme. All the transmitters (Tx) use the same laser source as the optical carrier (OC), which is split by an 1:N optical power splitter.

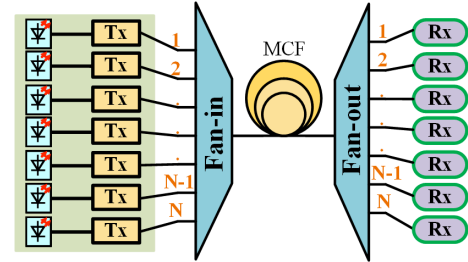


FIGURE 2. The laser non-shared scheme. Each transmitter (Tx) uses an independent laser source as the OC. There are unavoidable frequency offsets among the OCs.

B. MATHEMATICAL MODEL OF WC-MCF BASED IM/DD SYSTEMS

Based on [19], to model the WC-MCF-based short reach IM/DD systems, two cores are considered in the analysis: (i) the interfering core is used to generate the XT signal, and (ii) the signal core is used to evaluate signal performance and XT impact. After transmission over MCF, the Jones vector of the optical signal at the output of the signal core, $\mathbf{e}_0(t)$, can be expressed as:

$$\mathbf{e}_0(t) = \left[\left(A_{t,x} + ms_{t,x} \right) e^{j\omega t} + \left(A_{XT,x} + ms_{XT,x} \right) e^{j(\omega + \Delta\omega)t} \right] \mathbf{u}_x + \left[\left(A_{XT,y} + ms_{XT,y} \right) e^{j(\omega + \Delta\omega)t} \right] \mathbf{u}_y \quad (1)$$

where $A_{t,x}$ is the OC's slowly varying envelope amplitude of the signal core with the phase noise caused by laser linewidth

taken into consideration. $s_{t,x}$ is the data signal of the signal core which varies along time and the mean of $s_{t,x}$ is zero. The maximum modulus of $s_{t,x}$ is assumed to be equal to the modulus of the OC ($A_{t,x}$). m is the modulation depth and ranges from 0% to 100%. When the modulation depth is 0%, no signal is modulated on the OC. When the modulation depth is 100%, $s_{t,x}$ is fully modulated on the OC. $A_{XT,a}$ is the XT component amplitude originating from the OC of the interfering core in the polarization direction \mathbf{u}_a (with $a = x$ or $a = y$). $s_{XT,a}$ is the XT component originating from the data signal of the interfering core in the polarization direction \mathbf{u}_a . ω and $\omega + \Delta\omega$ are the angular frequency of the OC in the signal core and in the interfering core, respectively. j represents the imaginary unit. t represents time.

According to the analysis of Eq. (2) in [19], the power of the beating of the XT originating from the OC with the XT originating from data signal (OCXT-SXT), and the power of the beating of the XT originating from the data signal with itself (SXT-SXT) are negligible. However, when there is a frequency offset $\Delta\omega$ between the OCs, the OC-OCXT term, defined as the beating between the OC transmitted in the signal core and the XT originating from the OC in the interfering core, cannot be neglected. The OC-OCXT term can be expressed as [19]:

$$\begin{aligned} OC - OCXT &= 2\Re \left\{ A_{t,x} e^{j\omega t} \left[A_{XT,x} e^{j(\omega + \Delta\omega)t} \right]^* \right\} \\ &= 2\Re \left\{ A_{t,x} A_{XT,x}^* e^{-j\Delta\omega t} \right\} \end{aligned} \quad (2)$$

where z^* represents the conjugate of z . $\Re(x)$ represents the real part of x . Based on (2), it can be observed that the phase noise caused by laser linewidth and the frequency offset between OCs both can make the frequency components of the OC-OCXT term locate in band. Typically, the laser linewidth of $A_{t,x}$ and $A_{XT,x}$ are less than several MHz. The frequency offset between OCs is less than several gigahertz. The frequency components of the OC-OCXT term at low-frequency can be filtered out or equalized depending on the modulation format [19], the properties of DC-block, or the equalization algorithms of the receiver. The impact of the frequency components at higher-frequency will be studied comprehensively in this work.

The S-OCXT term is the beating of the data signal in the signal core with the XT originating from the OC transmitted in the interfering core, which can be expressed as:

$$\begin{aligned} S - OCXT &= 2\Re \left\{ m s_{t,x} e^{j\omega t} \left[A_{t,x} e^{j(\omega + \Delta\omega)t} \right]^* \right\} \\ &= 2m\Re \left\{ s_{t,x} A_{t,x}^* e^{-j\Delta\omega t} \right\} \end{aligned} \quad (3)$$

The OC-SXT term is the beating between the OC in the signal core and the XT originating from the data signal transmitted in the interfering core, which can be expressed as:

$$\begin{aligned} OC - SXT &= 2\Re \left\{ A_{t,x} e^{j\omega t} \left[m s_{XT,x} e^{j(\omega + \Delta\omega)t} \right]^* \right\} \\ &= 2m\Re \left\{ A_{t,x} s_{XT,x}^* e^{-j\Delta\omega t} \right\} \end{aligned} \quad (4)$$

The power of the OC-OCXT term and the power of the S-OCXT term fluctuate seriously as $|A_{XT,x}|^2$ can change slowly by more than 20 dB with time due to its narrow bandwidth [8]. Because the power of the OC is much higher than the power of the data signals ($|A_{t,x}|^2 \gg |s_{t,x}|^2$), the power of the OC-OCXT term is much higher than the power of the OC-SXT term and the power of the S-OCXT term when $A_{XT,x}$ is large. Therefore, we define the CBI as the combined effect of the intercore XT and the frequency offset between the OCs, mainly consisting of the OC-OCXT term, the OC-SXT term and the S-OCXT term. Further, the OC-OCXT term always dominates the CBI due to the much larger OC power.

In summary, the detected data signal without the DC component at the output of the signal core can be approximated by:

$$\begin{aligned} \frac{i(t)}{R_\lambda} &\approx 2m\Re \left\{ A_{t,x} s_{t,x}^* \right\} + \left| m s_{t,x} \right|^2 + 2\Re \left\{ A_{t,x} A_{XT,x}^* e^{-j\Delta\omega t} \right\} \\ &\quad + 2m\Re \left\{ A_{t,x} s_{XT,x}^* e^{-j\Delta\omega t} \right\} + 2m\Re \left\{ s_{t,x} A_{XT,x}^* e^{-j\Delta\omega t} \right\} \end{aligned} \quad (5)$$

where R_λ is the photo diode (PD) responsivity and $i(t)$ is the output current of the PD.

III. EXPERIMENTAL RESULTS

In this section, we first measure the carrier beating phenomena for the laser shared scheme and the laser non-shared scheme. Obvious carrier beating phenomena can be observed when the laser source has frequency dither. The related results are used to verify the proposed new laser model in Section IV. Then, we measure the CBI for a real WC-MCF-based transmission link using 10 GBaud PAM-4. Obvious SNR degradation caused by the CBI can be observed for the laser shared scheme and the laser non-shared scheme.

A. CARRIER BEATING PHENOMENON INDUCED BY TWO INDEPENDENT LASER SOURCES

Fig. 3 shows the experimental setup for measuring the carrier beating phenomenon of the laser non-shared scheme. Two laser sources are considered for the measurement with a 50:50 optical coupler to mix the optical waves. We use two variable optical attenuators (VOAs, VOABlade, coherent solutions) to adjust the input power of the PD. The polarization controller (PC, FPC560, Thorlabs) is used to align the polarization states before the 50:50 optical coupler. The optical source is a 4-channel thermally tuned external cavity laser (ECL, LaserBlade, coherent solutions). The laser uses a small FM dither as part of its wavelength-locking mechanism. The dither is always on and applies a slow back-and-forth adjustment of the center wavelength (± 48 MHz at 888 Hz) while maintaining an instantaneous laser linewidth (integration time 1 ms) of <100 kHz [29]. The frequency uncertainty and the frequency stability of the laser are ± 2.5 GHz and ± 0.3 GHz, respectively. The wavelengths of the two lasers are all set to 1550 nm with 13 dBm output power.

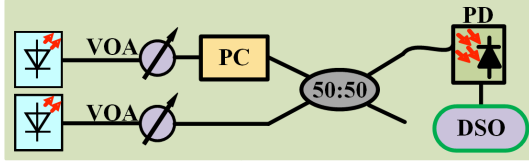


FIGURE 3. Experimental setup for measuring carrier beating phenomenon caused by two independent laser sources. Acronyms: VOA – variable optical attenuator, PC – polarization controller, PD – photo diode, DSO – digital storage oscilloscope.

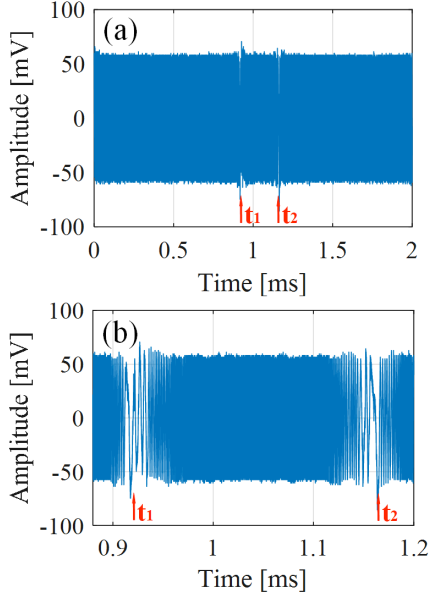


FIGURE 4. (a) Measured waveform of DSO, where t_1 and t_2 indicate times of 0.91 ms and 1.18 ms, respectively. (b) Detailed waveform from t_1 to t_2 . The beating becomes slow around t_1 and t_2 because of the lower frequency offset between the two lasers.

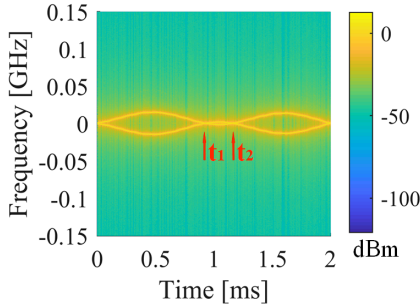


FIGURE 5. The instantaneous frequency (IF) spectrum of Fig. 4(a) calculated by the short-time Fourier transform (STFT). The dominant frequency components at t_1 and t_2 are close to zero, which means that the beating is slow at t_1 and t_2 .

The input power of PD (PIN with 10 GHz 3-dB bandwidth) is set to -4.0 dBm adjusted by the two VOAs. The sampling rate is 5 GSa/s of the digital storage oscilloscope (DSO, Labmaster 10Zi-A, Lecroy).

Fig. 4(a) shows the measured waveform acquired by the DSO with time length of 2 ms. The detailed waveform from 0.9 ms to 1.2 ms is shown in Fig. 4(b). It can be observed that the beating becomes slow at times t_1 (approximately 0.91 ms)

and t_2 (approximately 1.18 ms) and fast at other times. As the beating speed changes with time, the short-time Fourier transform (STFT) method [30] is used to analyze the instantaneous frequency (IF) spectrum of the waveform acquired by the DSO. We use a rectangular window to acquire data for each block. The block size of the fast Fourier transform (FFT) and the time interval of each FFT block are 2^{14} and 1.0 μ s, respectively. The time interval can be smaller than 1.0 μ s to increase the time resolution. The FFT block size can be set larger to increase the frequency resolution, but the time resolution simultaneously decreases. The time resolution and frequency resolution corresponding to an FFT block size of 2^{14} with 5 GSa/s are 3.3 μ s and 0.31 MHz, respectively. Therefore, it is difficult to analyze the phase noise caused by the laser linewidth because the frequency resolution is much higher than the laser linewidth (<100 kHz). However, the beating properties in Fig. 4 can be well analyzed.

Fig. 5 shows the evolution of the IF spectrum of Fig. 4(a). It can be observed that the dominant frequency components are close to zero at times t_1 and t_2 , which means that the beating is slow at times t_1 and t_2 . We can conclude that Fig. 5 can accurately describe the time-frequency characteristics of Fig. 4(a). Based on Fig. 5, the evolution of the main frequency component with time can be fitted by a trigonometric function with a 6 MHz frequency bias. The frequency dither range and the frequency dither period are approximately 12 MHz (± 6 MHz) and 1.2 ms, respectively. The beating speed is far larger than the beating caused by the phase noise of laser. Additionally, the estimated frequency dither period is in good agreement with the dither period of 1.13 ms (888 Hz in [29]). Therefore, it can be concluded that the measured beating waveform is caused by the laser dithering, rather than the laser phase noise. The discrepancy in the frequency dither range is discussed in Section IV.A.

B. CARRIER BEATING PHENOMENON INDUCED BY TIME DELAY

Fig. 6 shows the experimental setup for measuring the carrier beating phenomenon of the laser shared scheme. We use a 50:50 optical coupler to simulate the optical power splitter in Fig. 1. The other 50:50 optical coupler is used for the optical wave mixing. A section of standard single mode fiber (SSMF) is added to one path of the Mach-Zehnder interferometer (MZI) with the fiber length of L_{SMF} . The DSO's sampling rate is 5 GSa/s. The input power of the PD is 0 dBm. The wavelength and the output power of the laser are 1550 nm and 13 dBm, respectively.

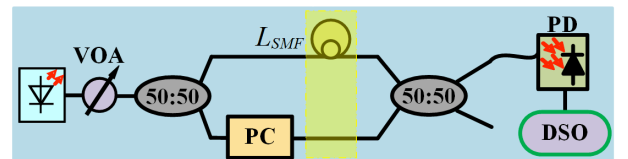


FIGURE 6. Experimental setup for measuring the carrier beating phenomenon caused by time delay. L_{SMF} is the length of a section of

standard single mode fiber (SMF) which de-correlates the signals of two paths.

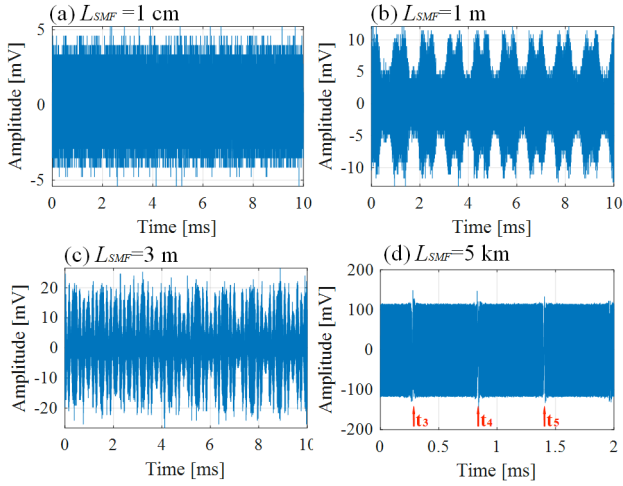


FIGURE 7. Measured waveforms of DSO with different fiber lengths L_{SMF} . The signals of two paths are fully decorrelated by 5 km SMF with a maximum amplitude of 100 mV. At times t_3 , t_4 , and t_5 , the beating becomes slow similar to that at t_1 and t_2 in Fig. 4.

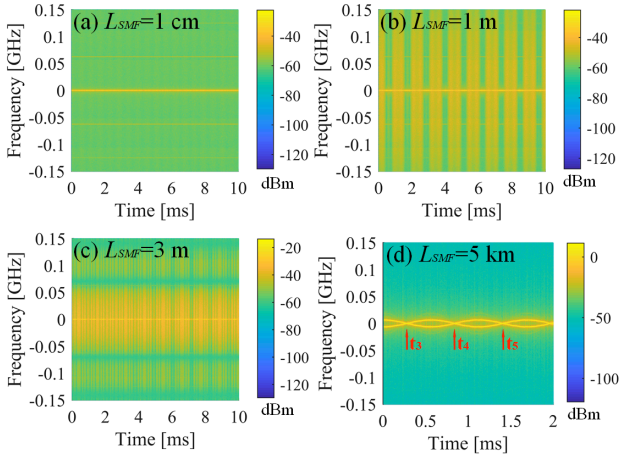


FIGURE 8. The IF spectrum of Fig. 7 calculated by STFT. The dominant frequency components at t_3 , t_4 and t_5 are close to zero.

Fig. 7 illustrates the waveform acquired by the DSO with different SMF lengths. When $L_{SMF} = 1$ cm, there is only the background noise of the DSO. With increasing SMF length, the beating grows stronger. When $L_{SMF} = 5$ km, the beating is as strong as that shown in Fig. 4(a). We can also observe that the beating slows at times t_3 , t_4 , and t_5 . Fig. 8 shows the corresponding IF spectrum of Fig. 7. Because we use one laser source, there is no frequency bias. The frequency dither range and the frequency dither period are approximately 10 MHz and 1.2 ms, respectively. The discrepancy in the frequency dither range is also discussed in Section IV.A.

C. MEASUREMENT OF CROSSTALK INDUCED CARRIER BEATING IMPAIRMENT

Fig. 9 shows two transmission setups, which are Tx1 (the laser shared scheme) and Tx2 (the laser non-shared scheme). We use a 3.5-km 7-core homogeneous step-index WC-MCF. The attenuation of each core is approximately 0.2 dB/km at

1550 nm. The chromatic dispersion of each core is 16.7 ps/nm/km at 1550 nm. The average core pitch and the cladding diameter of the WC-MCF are 41.5 μm and 150.0 μm , respectively. The estimated inter-core XT level is -11.1 dB/100 km [9]. The measured walk-off between core 1 and core 5 is 1.3 ps/m. The fan-in/fan-out device is manufactured using fused-tapering technology with the worst XT being less than -60 dB [31]. The average insertion loss is approximately 1 dB for each device with a variation of 0.5 dB. The decorrelation time of XT should be several minutes according to [32].

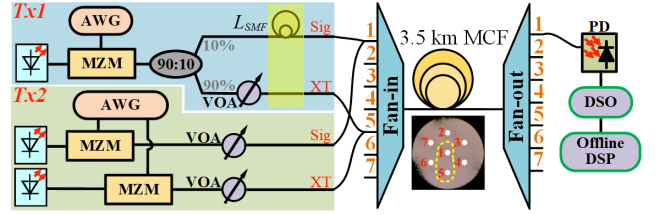


FIGURE 9. Diagram of the experimental setup for measuring the carrier beating impairment (CBI). The estimated XT between cores is -11 dB/100 km. The walk-off between core 1 and core 5 is 1.3 ps/m. Tx1 represents to the laser shared scheme, and Tx2 represents to the laser non-shared scheme. Acronyms: AWG - arbitrary waveform generator, MZM - Mach-Zehnder modulator, DSP - digital signal processing.

The optical source is a 4-channel thermally tuned external cavity laser (ECL, LaserBlade, coherent solutions) with a maximum output power of 13.6 dBm. An arbitrary waveform generator (AWG, 65 GSa/s, M8195A, Keysight) and a 40-GHz Mach-Zehnder modulator (MZM, MX-LN-40, photline) are used to generate 10 GBaud PAM-4 optical signals with PRBS length of 2^{17} . A raised cosine pulse shaping filter with a roll-off factor of 0.18 is used for pulse shaping. Two MZMs are used for Tx2 with independent PAM-4 signals modulated. For both the transmission setups, core 1 (center core) is used as the signal core, and core 5 (one of the outer cores) is used as the interfering core to bring XT into core 1. We also use a 10-GHz PD and a DSO (40GSa/s, Labmaster 10Zi-A, Lecroy) to acquire the output optical signals of core 1 with -9 dBm optical power. Note that a T/2 symbol-spaced decision-directed least-mean-squares (DD-LMS) equalizer with 35 taps (only 12 non-zero taps) is used to compensate residual inter-symbol interference (ISI) [4, 33]. For Tx1, we use a section of SMF to decorrelate two channels' signals with a length of L_{SMF} . This setup is always used to ensure that the data signal in the interfering core is independent with the data signal in the signal core due to its convenience [19, 21, 22]. The wavelength of the laser source is set to 1550 nm. The output power of core 1 is -9.0 dBm. For Tx2, the wavelengths of the two lasers are also set to 1550 nm. The other VOA connected with the core 1 is to ensure that the output power is also -9.0 dBm.

We use the VOA connected to the interfering core to adjust XT level. To calibrate XT level, the 10 GBaud PAM-4 signal is always modulated to get a more stable short-term average crosstalk (STAXT) presented in [8]. For Tx1, when

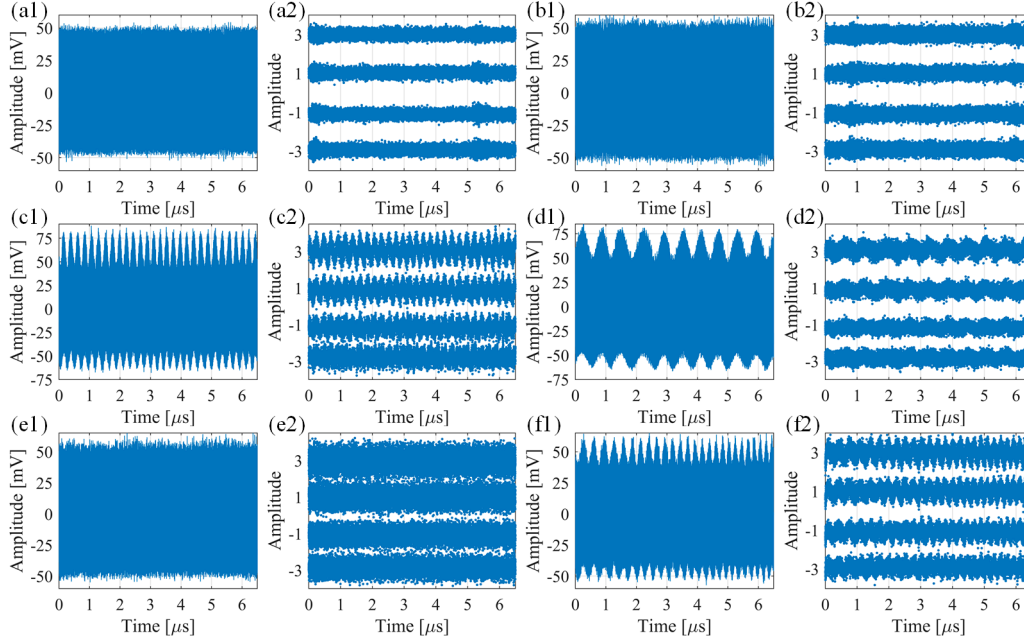


FIGURE 10. The received waveforms of the DSO (a1, b1, ..., f1) and the recovered PAM-4 signals after DD-LMS (a2, b2, ..., f2) for various conditions. (a): Tx1, XT level = -50 dB, $L_{SMF} = 1$ cm, and SNR = 23.2 dB; (b): Tx1, XT level = -20 dB, $L_{SMF} = 1$ cm, and SNR = 21.8 dB; (c): Tx1, XT level = -20 dB, $L_{SMF} = 5$ km, and SNR = 16.5 dB; (d): Tx1, XT level = -20 dB, $L_{SMF} = 5$ km, and SNR = 19.2 dB; (e): Tx2, XT level = -20 dB, and SNR = 16.0 dB; (f): Tx2, XT level = -20 dB, and SNR = 18.7 dB.

the VOA is set to 10.5 dB insertion loss, the output power of the signal core is -30.0 dBm when only the interfering core is injected optical signal. The measurement time is 300 s with the time interval of 0.65 s. In this situation, the average XT level is assumed as $-30.0 - (-9.0) = -21.0$ dB. For Tx2, the calibration of the XT level is the same as that for Tx1. It should be noted that the XT level is not re-calibrated during the experiment. The real XT level added on the signal core is affected by the time-dependence of the XT and the XT setting error can reach about several dB according to [8]. The signal performance fluctuation caused by the time-dependent XT is studied via numerous simulations in Section IV.B.

Fig. 10 shows the acquired waveforms with the sampling rate of 40 GSa/s and their corresponding recovered PAM-4 signals in various conditions. For example, Figs. 10(a1) and 10(a2) show one of the received waveforms and its corresponding recovered PAM-4 signals, respectively, for Tx1 with -50 dB XT when $L_{SMF} = 1$ cm. It can be observed that, the signals are recovered well when XT is small enough. The recovered SNR of Fig. 10(a2) is 23.2 dB without bit error. For each frame of recovered data (approximately 65000 symbols), the SNR is calculated according to the error vector magnitude (EVM) with a reference level of PAM-4 (± 1 and ± 3). Figs. 10(b1) and 10(b2) show one of the measured results for Tx1 with -20 dB XT when $L_{SMF} = 1$ cm. We can observe slight SNR degradation approximately 1.4 dB with the recovered SNR of 21.8 dB.

Figs. 10(c) and 10(d) are two samples with -20 dB XT for Tx1 when $L_{SMF} = 5$ km. When we change L_{SMF} to 5 km, the

envelope of the received waveform obviously fluctuates when the XT is -20 dB. The envelopes of the waveform in Figs. 10(c1) and 10(d1) show different patterns. The recovered SNRs of Figs. 10(c2) and 10(d2) are 16.5 dB and 19.2 dB, respectively. Comparing Figs. 10(d1) with 10(d2), we can observe that the DD-LMS almost compensate the fluctuations of the received waveforms. The reason should be that the updating step size of each tap in the DD-LMS equalizer is large enough and the estimated errors of adjacent symbols are identical. Therefore, reasonably increasing the updating step size and reducing the tap number should improve the tracking speed of the DD-LMS equalizer. Figs. 10(e) and 10(f) are two samples for Tx2 with -20 dB XT. The recovered SNRs of Figs. 10(e2) and 10(f2) are 16.0 dB and 18.7 dB, respectively. We can also observe an obvious pattern from Fig. 10(f1). The periods of the patterns for Figs. 10(c1), 10(d1) and 10(f1) are approximately 0.2 μ s, 0.6 μ s and 0.2 μ s, respectively. The corresponding beating frequencies are 5 MHz, 1.6 MHz and 5 MHz, respectively, which is far beyond the beating frequency caused by the laser linewidth (<100 kHz) [29]. This means that the OC-OCXT term causes the recovered signals' obvious fluctuations, rather than the OC-SXT term and the S-OCXT term. In addition, we can conclude that the OC-OCXT term dominates the CBI when there is large OC frequency offset. It should be noted that there seems to be no obvious pattern in Fig. 10(e1) because the frequency offset between the OCs in Fig. 10(e1) is too large and the period of the carrier beating is too small to be distinguished directly from the figure.

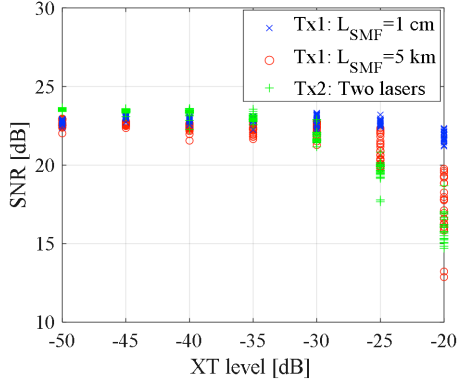


FIGURE 11. SNR degradation with different XT levels for Tx1 and Tx2. The CBI causes additional SNR degradation for Tx1 with $L_{SMF}=5$ km and Tx2.

Furthermore, we measured the system performances for three transmission setups, which are as follows: (setup-A) Tx1 with $L_{SMF} = 1$ cm, (setup-B) Tx1 with $L_{SMF} = 5$ km, and (setup-C) Tx2. There is no CBI for setup-A, but for setup-B and setup-C, CBI always exists. We change the XT level from -50 dB to -20 dB using the VOA as before. In each case, the signals are measured 25 times at time interval approximately 30 s. Fig. 11 shows the measurement results. The blue cross marker shows the SNR degradation with setup-A. We can observe approximately 1-dB SNR degradation when the XT level reaches -20 dB. The red circle marker and green pulse sign marker demonstrate the measurement results for setup-B and setup-C, respectively. In both setup-B and setup-C, the SNR ranges from 13 dB to 20 dB with -20 dB XT.

The time interval (30 s) is smaller than the decorrelation time of the XT. Therefore, 25 measurements are unable to show the real SNR fluctuations. However, the SNR degradation from Fig. 10(c) to Fig. 10(f) is actually caused by the OC-OCXT term of the CBI as discussed above. Additionally, the time-dependence of XT affects the power of the OC-OCXT term, causing SNR fluctuation for different data frames. To characterize the SNR fluctuation comprehensively, it is reasonable to investigate the system performance via simulation with enough uncorrelated samples as shown in Section IV.

In summary, the CBI consists of the OC-OCXT term, the OC-SXT term and the S-OCXT term. For transmitter setup Tx1, two conditions need to be satisfied when the OC-OCXT term dominates the CBI for PAM-4 transmission: (i) the laser source has frequency dither and the frequency dither range is large enough, and (ii) the SSMF should be longer to introduce enough OC's frequency offset between the signal core and the interfering core. For transmitter setup Tx2, only one of the two conditions need to be satisfied when the OC-OCXT term dominates the CBI: (i) there is frequency offset between the two lasers when the laser does not use frequency dither, which has been investigated in [33], and (ii) the laser uses frequency dither to lock the optical wavelength to introduce

large OC frequency offset. Further discussion via simulation is presented in Section V.

IV. SIMULATION RESULTS

A. MODELING OF LASER WITH FREQUENCY DITHER

To the best of our knowledge, no laser model with frequency dither described has been proposed for optical fiber transmission simulations. Therefore, we build a new laser model with frequency dither taken into consideration. The output electric field $E(t)$ of the laser can be expressed as:

$$E(t) = \sqrt{P} \exp \left(j\phi_l + j \int_0^t \underbrace{\omega_l(\tau)}_{\text{linewidth}} d\tau + j \int_0^t \underbrace{\left[\frac{2\pi F_d \sin\left(\frac{2\pi}{T} \tau + \phi_d\right) + 2\pi\Delta f}{\text{frequency dither}} \right]}_{\text{frequency dither}} d\tau \right) \quad (6)$$

where $E(t)$ and P represent the complex amplitude of the electric field of a continuous wave (CW) laser source and its output power, respectively. ϕ_l represents the initial random phase according to the uniform distribution within $[0, 2\pi]$. $\int_0^t \omega_l(\tau) d\tau$ represents the optical phase fluctuation caused by laser linewidth, which is modeled using a Gaussian random variable with a variance of $2\pi\Delta f_l$, corresponding to the full width at half maximum (FWHM) linewidth Δf_l [35]. Fig. 12 shows the fitting results of laser linewidth according to Lorentz fitting. The target linewidth is 1.0 MHz with the sampling rate and samples of 1 GSa/s and 1 MSa, respectively. Based on the power spectrum density (PSD) of $E(t)$, the fitted linewidth caused by the frequency fluctuation is 1.003 MHz with the R^2 of 0.990. Δf represents the center optical frequency offset. Based on the measurement results of Fig. 5, Fig. 8 and the specification sheet [29], we consider the laser frequency to be dithered by a trigonometric function with range, period, and initial phase of F_d , T , and ϕ_d , respectively. ϕ_d can be treated as uniformly distributed within $[0, 2\pi]$.

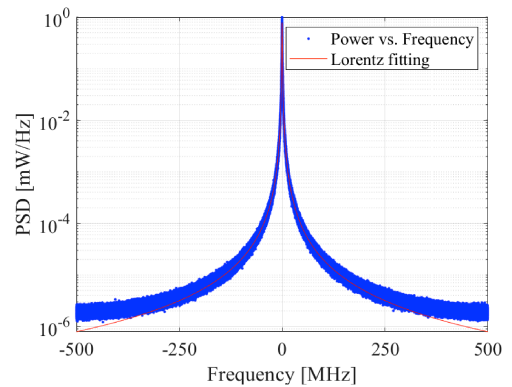


FIGURE 12. Measured linewidth fitted by Lorentz function with the R^2 of 0.990. The target linewidth is 1.0 MHz. The fitted linewidth is 1.003 MHz.

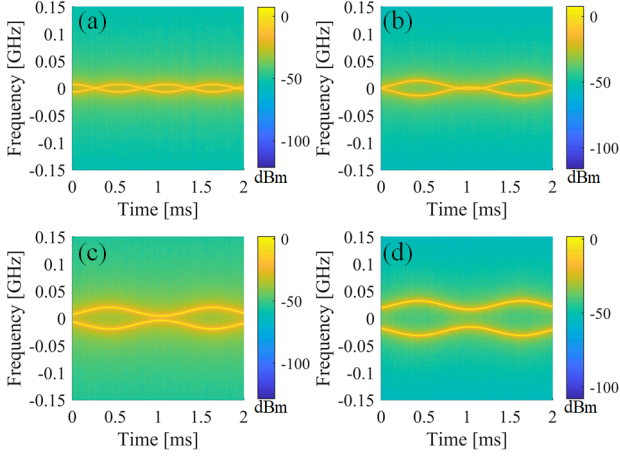


FIGURE 13. (a) The IF spectrum with one shared laser decorelated by 5 km SMF corresponding to Fig. 6. (b), (c) and (d) are the IF spectra with two independent lasers with 6 MHz, 12 MHz, and 24 MHz center optical frequency offset, respectively.

According to square law detection with a single polarization state taken into consideration, the received beating signal $S(t)$ can be expressed by:

$$S(t) = |E_1(t) + E_2(t)|^2 \quad (7)$$

where E_1 and E_2 are the complex amplitudes of the electric fields of the two lasers. Fig. 13 demonstrates the IF spectra calculated by the STFT in different situations for parameter calibration of (6). To make Fig. 13(a) the same as Fig. 8(d), the electric field E_2 needs to be delayed 25 μ s (time delay of 5 km SMF with 2×10^8 m/s group velocity assumed) of E_1 for Tx1. Based on the results of Figs. 5 and 8(d), we set frequency dither period T to approximately 1.2 ms, which is in good agreement with the specification sheet [29]. The center optical frequency offset Δf is set to zero. To reach the 10 MHz frequency range as shown in Fig. 8(d), the frequency dither range F_d needs to be set as 50 MHz, which is also in good agreement with the specification sheet [29]. Figs. 13(b) to 13(d) show the IF spectra for Tx2. To make Fig. 13(b) the same as Fig. 5, the center optical frequency offset needs to be 6 MHz for Tx2. The difference between the ϕ_d of the two lasers is set to $\pi/20$, which decreases the beating frequency range from 100 MHz (± 50 MHz) to 10 MHz. Figs. 13(c) and 13(d) are the IF spectra with two independent lasers and 12 MHz, and 24 MHz center optical frequency offset, respectively. The results indicate that there is a small center optical frequency offset Δf for Tx2 even when the lasers are set to the same wavelength. When the difference in ϕ_d is equal to π , the beating frequency range is equal to 100 MHz (± 50 MHz).

B. SIMULATION RESULTS FOR CARRIER BEATING IMPAIRMENT

Based on the above laser model and our previous WC-MCF channel model [34], we can simulate the experimental setup (Fig. 9) based on MATLAB 2017a. An ideal modulator and

an ideal PD are modeled according to the related models in [35]. The modulation depth is set to 65%. The optical properties of WC-MCF are set according to the measurement results. The center optical frequency of laser source is set to 193.1 THz, and the sampling rate of simulation is 40 GSa/s with a frame length of 2^{17} symbols for 10 GBaud PAM-4 signals. We use a virtual ideal VOA to adjust the XT level by controlling the input power of the interfering core. To achieve a target initial SNR, we add Gaussian white noise to the electric PAM-4 signals. We run the simulation 500 times in each case, where the bit stream, the random parameters of MCF, ϕ_d , ϕ_l , and ω_l are all re-generated independently. This ensures that each simulation is completely decorrelated with the others. In the time window of each simulation, the XT is assumed to be unchanged with time. Because the time window is approximately 13.1 μ s which is much smaller than the decorrelation time of XT.

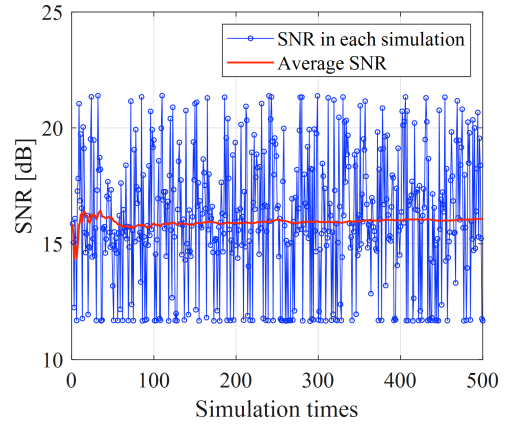


FIGURE 14. The SNR of each simulation with 500 times for setup-C with -20 dB XT. The average SNR becomes stable when the number of simulation times is larger than 300. There are enough samples with the maximum SNR or the minimum SNR with 500 times simulation.

Fig. 14 shows the SNR of each simulation for setup-C with -20 dB XT. The average SNR becomes stable when the number of simulation times is larger than 300. The minimum SNR is approximately 11.6 dB because of the estimated lower bound by using EVM. There are more than 15 samples with the maximum SNR and more than 40 samples with the minimum SNR within 500 times simulation. This indicates that 500 times simulations can describe the system's long-term performance. Fig. 15 shows the simulation results for SNR degradation. For setup-B, Tx1 with $L_{SMF} = 5$ km, and setup-C, Tx2, we can observe that the SNR fluctuates from 12 dB to 22 dB with -20 dB XT. For setup-A, Tx1 with $L_{SMF} = 1$ cm, the maximum tolerable XT level (at worst 1-dB SNR degradation) for PAM-4 transmissions is approximately -25 dB. However, for setup-B and setup-C, the maximum tolerable XT level (at worst 1-dB SNR degradation) decreases to approximately -45 dB. This result indicates that the XT level of WC-MCF should be designed to be 20 dB less when there is CBI for a real WC-MCF-based PAM-4

transmission link. Because the recovered SNR for a real WC-MCF transmission link may be smaller than 23 dB, the maximum tolerable XT for all the setups could be changed [33]. Comparing Fig. 11 with Fig. 15, we can observe that there are some discrepancies between the simulation results and the experimental results. The measurement SNRs of Tx2 (green plus marker) in Fig. 11 are relatively concentrated. But the simulation results of Tx2 in Fig. 15 are more dispersed. This discrepancy is caused by the insufficient samples of experiment and the time-dependence of the XT. In addition, the modulation depth has obvious effect on the SNR degradation caused by the CBI, which is presented in Section V. Because the SNR degradation caused by the CBI depends on the parameters of the system setups, we suggest that a specific analysis should be conducted for different system setups.

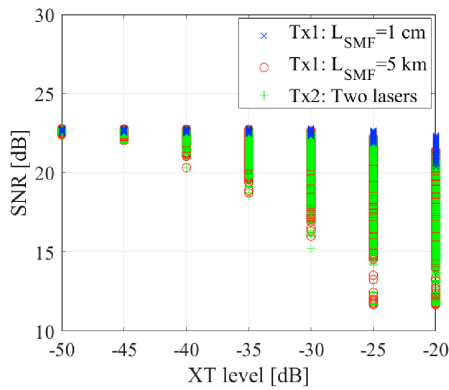


FIGURE 15. Simulation results for SNR degradation caused by different XT levels w/wo CBI. CBI causes additional SNR degradation at the -25 dB XT level.

Fig. 15 shows the simulation results for SNR degradation. For setup-B, Tx1 with $L_{SMF} = 5$ km, and setup-C, Tx2, we can observe that the SNR fluctuates from 12 dB to 22 dB with -20 dB XT. For setup-A, Tx1 with $L_{SMF} = 1$ cm, the maximum tolerable XT level (at worst 1-dB SNR degradation) for PAM-4 transmissions is approximately -25 dB. However, for setup-B and setup-C, the maximum tolerable XT level (at worst 1-dB SNR degradation) decreases to approximately -45 dB. This result indicates that the XT level of WC-MCF should be designed to be 20 dB less when there is CBI for a real WC-MCF-based PAM-4 transmission link. Because the recovered SNR for a real WC-MCF transmission link may be smaller than 23 dB, the maximum tolerable XT for all the setups could be changed [33]. Comparing Fig. 11 with Fig. 15, we can observe that there are some discrepancies between the simulation results and the experimental results. The measurement SNRs of Tx2 (green plus marker) in Fig. 11 are relatively concentrated. But the simulation results of Tx2 in Fig. 15 are more dispersed. This discrepancy is caused by the insufficient samples of experiment and the time-dependence of the XT. In addition, the modulation depth has obvious effect on the

SNR degradation caused by the CBI, which is presented in Section V. Because the SNR degradation caused by the CBI depends on the parameters of the system setups, we suggest that a specific analysis should be conducted for different system setups.

V. DISCUSSION

Based on the above simulation, we can investigate the impact of the frequency dither range F_d , the frequency dither period T , the modulation depth m , and the walk-off between the cores of MCF [34] on the CBI, which is difficult to measure via experiments. Toward high speed optical transmissions, we increase the baud rate from 10 GBaud to 56 GBaud with an ideal chromatic dispersion compensation module added on the receiver side similar to [4]. We choose the laser non-shared scheme (Tx2) as the simulation setup with no center optical frequency offset. Under each condition, the simulation is repeated 500 times, where the bit stream, random parameters of MCF, ϕ_d , ϕ_l , and ω_l are all regenerated independently. The XT level is set to -40 dB. In the time windows of each simulation, the XT is assumed to be unchanged with time. The other parameters are as the same as the parameters of setup-C in Fig. 15. Each simulation result is drawn as a blue cross marker.

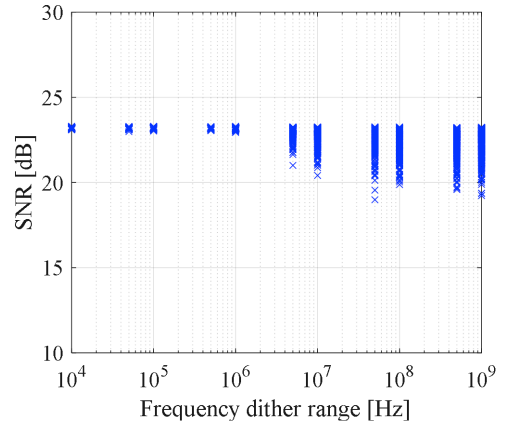


FIGURE 16. The effect of the frequency dither range on the CBI via simulation results.

Fig. 16 shows the simulation results for the effect of the frequency dither range on the CBI. The frequency dither range changes from 10^4 Hz to 10^9 Hz. It can be observed that the SNR degradation caused by the CBI can be neglected if the frequency dither range is less than 1.0 MHz. This is in agreement with the conclusion in [33]. The frequency offset of the lasers should be less than 1.0 MHz when the lasers does not have frequency dither. The small frequency offset does not cause additional SNR degradation because the tracking speed of the DD-LMS can keep up with the signal fluctuations caused by the CBI. Therefore, the random OC frequency offset of each frame data is one of the sources causing SNR fluctuation and the other reason is the time-dependence of XT. Fig. 17 shows the simulation

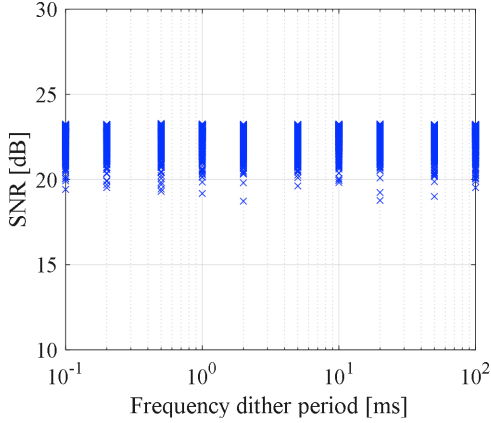


FIGURE 17. The effect of the frequency dither period on the CBI via simulation results.

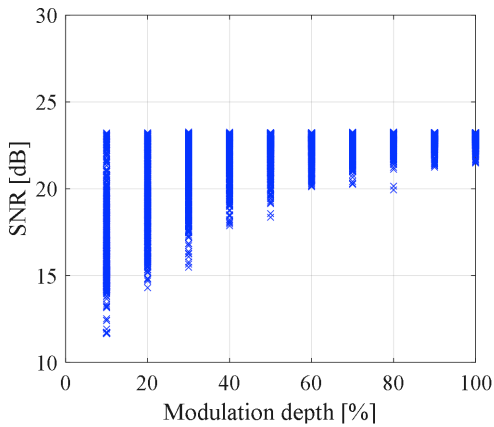


FIGURE 18. The effect of the modulation depth on the CBI via simulation results.

results of the effect for the frequency dither period on the CBI. The frequency dither period changes from 0.1 ms to 100 ms. It can be concluded that the frequency dither period has no influence on the CBI.

Fig. 18 shows the simulation results for the effect of the modulation depth on the CBI. The modulation depth changes from 10% to 100%. It can be observed that the modulation depth should be as large as possible to weaken the SNR degradation because higher modulation depth yields larger power of the OC-S term (the beating of the OC and the data signal in the signal core) in (4). However, higher modulation depth does change the power of the OC-OCXT term. When the OC-OCXT dominates the CBI, the effect of the OC-SXT term is relatively small. However, for a real modulator, the modulation depth cannot be 100% due to the nonlinear transfer function of modulation. Fig. 19 shows the simulation results for the impact of the walk-off between the cores on the CBI. The walk-off changes from 0 ps/m to 2.0 ps/m. It can be concluded that the walk-off has no influence on the CBI, because the walk-off has no effect on the characteristics of $A_{XT,x}$ in (2). This seemingly contradicts the conclusion in [20], which states that

significantly different IM/DD system performance can be observed for low and high walk-offs. The reason is that the OC-SXT term is the main XT component in [20] because the same OC's optical frequency of the lasers. But the OC-OCXT term is dominant XT component in Fig. 19 due to the OC's optical frequency offset caused by the laser frequency dither. The effect of walk-off and laser linewidth on transmission performance can be found in [33] when there is no CBI.

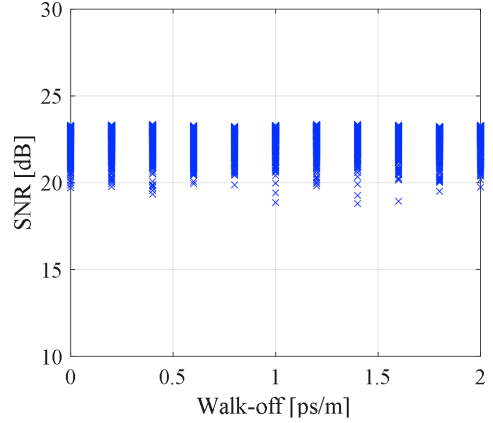


FIGURE 19. The effect of the walk-off between cores on the CBI via simulation results.

VI. CONCLUSION

We measured the combined effect of intercore XT and the frequency offset between optical carriers, which is defined as the CBI. The OC-OCXT term always dominates the CBI rather than the OC-SXT term and the S-OCXT term. The measured frequency dither range and the frequency dither period of the ECL are approximately 50 MHz and 1.2 ms, respectively, which is in good agreement with the specification sheet [29]. We experimentally confirmed the obvious SNR degradation caused by the CBI. We built a new laser model that can describe the optical properties of a laser source with frequency dither technology. Based on the simulation results, the maximum tolerable XT level (at worst 1-dB SNR degradation) decreases to approximately -45 dB when there is CBI for PAM-4 transmissions. The simulation results indicate that there is no need to take the CBI into consideration for the laser shared transmitter setup if an integrated transmitter is utilized for WC-MCF short-reach IM/DD transmissions in the future because the time delay should be small enough. However, when we apply the laser non-shared scheme for transmission, the optical frequency of the lasers should be carefully controlled to avoid the CBI, because the optical frequency of the laser changes with temperature and time. Otherwise, the XT level of the WC-MCF should be designed to be much smaller to avoid SNR degradation caused by the CBI. The analysis for the CBI caused by multiple cores or the CBI in heterogeneous WC-MCF will be performed in the future.

ACKNOWLEDGMENTS

Jiajia Zhao would like to thank Dr. Chen Yang and Dr. Weijun Tong from Yangtze Optical Fiber and Cable Joint Stock Limited Company (YOFC) R&D Center for their support with the multicore fiber. Jiajia Zhao would like to thank Jiajun Zhou for helpful discussions and assistance with the experiments. Lin Gan would like to thank Yizhao Chen for insightful suggestions and discussions.

REFERENCES

- [1] S. Zhang, *et al.*, "Quantum Communication Networks and Trust Management: A Survey," *CMC-Computers, Materials & Continua*, vol. 61, no. 3, pp. 1145-1174, 2019.
- [2] B. Jo, *et al.*, "Efficient Computation Offloading in Mobile Cloud Computing for Video Streaming Over 5G," *CMC-Computers, Materials & Continua*, vol. 61, no. 2, pp. 439-463, 2019.
- [3] T. Hayashi *et al.*, "MULTI-CORE FIBERS FOR DATA CENTER APPLICATIONS," presented at the *45th European Conference on Optical Communication (ECOC)*, Dublin, Republic of Ireland, Step. 22-26, 2019.
- [4] X. Pang, *et al.*, "7×100 Gbps PAM-4 Transmission over 1-km and 10-km Single Mode 7-core Fiber using 1.5- μm SM-VCSEL," in *Proc. the 43th Optical Fiber Communications Conference and Exposition (OFC)*, San Diego, CA, USA, 2018, paper: M11.4.
- [5] R. Lin, *et al.*, "Real-time 100 Gbps/ λ /core NRZ and EDB IM/DD transmission over multicore fiber for intra-datacenter communication networks," *Opt. Express*, vol. 26, no. 8, pp. 10519-10526, Apr. 2018.
- [6] T. Fujisawa, *et al.*, "Crosstalk Analysis of Heterogeneous Multicore Fibers Using Coupled-Mode Theory," *IEEE Photonics Journal*, vol. 9, no. 6, pp. 1-8, Oct. 2017.
- [7] R. O. J. Soeiro, T. M. F. Alves and A. V. T. Cartaxo, "Dual Polarization Discrete Changes Model of Inter-Core Crosstalk in Multi-Core Fibers," *IEEE Photonics Technol. Lett.*, vol. 29, no. 16, pp. 1395-1398, Aug. 2017.
- [8] G. Rademacher, *et al.*, "Crosstalk dynamics in multi-core fibers," *Opt. Express*, vol. 25, no. 10, pp. 12020-12028, May 2017.
- [9] L. Gan, *et al.*, "Investigation of channel model for weakly coupled multicore fiber," *Opt. Express*, vol. 26, no. 5, pp. 5182-5199, Mar. 2018.
- [10] T. F. Alves and A. V. T. Cartaxo, "Decorrelation Bandwidth of Intercore Crosstalk in Weakly-Coupled Multicore Fibers with Multiple Interfering Cores," *J. of Lightwave Technol.*, vol. 37, no. 3, pp. 744-754, Feb. 2019.
- [11] R. O. J. Soeiro, T. M. F. Alves and A. V. T. Cartaxo, "Impact of Longitudinal Variation of the Coupling Coefficient Due to Bending and Twisting on Inter-Core Crosstalk in Weakly-Coupled MCFs," *J. of Lightwave Technol.*, vol. 36, no. 18, pp. 3898-3911, Jul. 2018.
- [12] H. Yuan, *et al.*, "Experimental Investigation of Static and Dynamic Crosstalk in Trench-Assisted Multi-Core Fiber," in *Proc. the 44th Optical Fiber Communications Conference and Exposition (OFC)*, San Diego, CA, USA, 2019, paper: W4C.2.
- [13] R. S. Luis, *et al.*, "Crosstalk Impact on a 535 Tb/s 172 km Transmission Using a Homogeneous 19-Core Multicore Fiber," in *Proc. Conference on Lasers and Electro-Optics (CLEO)*, San Jose, CA, USA, 2018, paper: SM4C.1.
- [14] J. M. Gene and P. J. Winzer, "A Universal Specification for Multicore Fiber Crosstalk," *IEEE Photonics Technol. Lett.*, vol. 31, no. 9, pp. 673-676, May 2019.
- [15] V. Francois and F. Laramée, "Multicore fiber optimization for application to chip-to-chip optical interconnects," *J. Lightwave Technol.*, vol. 31, no. 24, pp. 4022-4028, Dec. 2013.
- [16] J. K. Mishra, V. Priye, and B. M. A. Rahman, "Error Probability Performance of a Short-Reach Multicore Fiber Optical Interconnect Transmission System," *Opt. Lett.*, vol. 40, no.19, pp. 4556-4559, Oct. 2015.
- [17] T. Hayashi, *et al.*, "125- μm -Cladding 8-core multi-core fiber realizing ultra-high-density cable suitable for O-band short-reach optical interconnects," in *Proc. the 40th Optical Fiber Communications Conference and Exposition (OFC)*, Los Angeles, CA, USA, 2015, paper: Th5C.6.
- [18] J. K. Mishra, B. M. A. Rahman, and V. Priye, "Rectangular Array Multicore Fiber Realizing Low Crosstalk Suitable for Next Generation Short Reach Optical Interconnects with Low Misalignment Loss", *IEEE Photonics Journal*, vol. 8, no. 4, pp. 1-14, Aug. 2016.
- [19] T. M. F. Alves, *et al.*, "Performance of adaptive DD-OFDM multicore fiber links and its relation with intercore crosstalk," *Opt. Express*, vol. 25, no. 14, pp. 16017-16027, Jul. 2017.
- [20] J. L. Rebola, *et al.*, "Outage Probability Due to Intercore Crosstalk in Dual-Core Fiber Links with Direct-Detection," *IEEE Photonics Technol. Lett.*, vol. 31, no. 14, pp. 1195-1198, Jul. 2019.
- [21] T. M. F. Alves, J. L. Rebola and A. V. T. Cartaxo, "Characterization of Crosstalk-Impaired OOK Signals in WC-MCF Systems with High and Low Skew×Bit Rate," presented at the *45th European Conference on Optical Communication (ECOC)*, Dublin, Republic of Ireland, Step. 22-26, 2019.
- [22] A. Udalvoics, *et al.*, "Inter-Core Crosstalk in Multicore Fibers: Impact on 56-Gbaud/ λ /Core PAM-4 Transmission," presented at the *44th European Conference on Optical Communication (ECOC)*, Roma, Italy, Step. 23-27, 2018.
- [23] R. S. Luis, *et al.*, "DYNAMIC CROSSTALK AND SKEW ON A 1.3 TB/S FULL-DUPLEX O-BAND SHORT REACH TRANSMISSION USING AN 8-CORE FIBER," presented at the *45th European Conference on Optical Communication (ECOC)*, Dublin, Republic of Ireland, Step. 22-26, 2019.
- [24] T. M. F. Alves, *et al.*, "Intercore crosstalk in direct-detection homogeneous multicore fiber systems impaired by laser phase noise," *Opt. Express*, vol. 25, no. 23, pp. 29417-29431, Nov. 2017.
- [25] J. L. Rebola, T. M. F. Alves, and A. V. T. Cartaxo, "Assessment of the combined effect of laser phase noise and intercore crosstalk on the outage probability of DD OOK systems," in *Proc. the 21th International Conference on Transparent Optical Networks (ICTON)*, Angers, France, 2019, paper: We.D1.4.
- [26] L. Gan, *et al.*, "Carrier Beating Impairment of PAM, CAP and DMT in Multicore Fiber Based IM/DD Systems," in *Proc. the 19th Asia Communications and Photonics Conference (ACP)*, Chengdu, Sichuan, China, 2019, paper: T3G.2.
- [27] C. Hoessbacher, *et al.*, "Optical Interconnect Solution With Plasmonic Modulator and Ge Photodetector Array," *IEEE Photonics Technol. Lett.*, vol. 29, no. 21, pp. 1760-1763, Nov. 2017.
- [28] P. Westbergh, J. S. Gustavsson and A. Larsson, "VCSEL Arrays for Multicore Fiber Interconnects With an Aggregate Capacity of 240 Gb/s," *IEEE Photonics Technol. Lett.*, vol. 27, no. 3, pp. 296-299, Feb. 2015.
- [29] Coherent Solutions, "LaserPXIe 1000 Series Specification Sheet," [Online]. Available: https://www.coherent-solutions.com/downloads/cs-specsheets/CS_LaserPXIe_1000_Series_Spec_Sheet_V1.03.3.pdf.
- [30] B. Boualem, "Heuristic Formulation of Time-Frequency Distributions," in *Time-Frequency Signal Analysis and Processing A Comprehensive Reference*, 2nd ed., UK: Elsevier 2016, ch. 2, sec. 3, pp. 76-77.
- [31] L. Gan, *et al.*, "Ultra-Low Crosstalk Fused Taper Type Fan-in/Fan-out Devices for Multicore Fibers", in *Proc. the 44th Optical Fiber Communications Conference and Exposition (OFC)*, San Diego, CA, USA, 2019, paper: Th3D.3.
- [32] T. M. F. Alves and A. V. T. Cartaxo, "Characterization of the stochastic time evolution of short-term average intercore crosstalk in multicore fibers with multiple interfering cores," *Opt. Express*, vol. 26, no. 4, pp. 4605-4620, Feb. 2018.
- [33] L. Gan, *et al.*, "Crosstalk Impacts on Homogeneous Weakly-Coupled Multicore Fiber Based IM/DD System", in *Proc. the 18th Asia Communications and Photonics Conference (ACP)*, Hangzhou, Zhejiang, China, 2018, paper: Su1D.8.

-
- [34] L. Gan, *et al.*, "Efficient Channel Model for Homogeneous Weakly Coupled Multicore Fibers," *IEEE Journal of Selected Topics in Quantum Electronics*, vol. 26, no. 4, pp. 1-11, May. 2019.
- [35] VPItransmissionMaker™ Optical Systems, *modules.chm*, [Online]. Available: https://vpiphotonics.com/Tools/DesignSuite/Demos/OS_ShortReach.php#app.